



Nonlinear low-velocity impact response of GRC beam with geometric imperfection under thermo-electro-mechanical loads

Wei Zhang · Li-Jia Guo · Yuewu Wang · Jia-Jia Mao  · Jianwei Yan

Received: 1 April 2022 / Accepted: 13 August 2022 / Published online: 29 August 2022
© The Author(s), under exclusive licence to Springer Nature B.V. 2022

Abstract This paper presents an investigation on thermo-electro-mechanical nonlinear low-velocity impact behaviors of the geometrically imperfect functionally graded (FG) graphene-reinforced composite (GRC) beam with surface-bonded piezoelectric layers. Both uniformly distributed and FG patterns of graphene nanoplatelets (GPLs) are considered along the thickness of the GRC host beam. The effective Young's modulus is calculated by the Halpin–Tsai model. The Poisson ratio and mass density are calculated by the rule of mixture. The modified nonlinear Hertz contact law is employed to predict the impact force between the spherical impactor and the geometrically imperfect GRC piezoelectric beam during impacting. By considering the first-order shear deformation theory and von Kármán nonlinear displacement–strain relationship, the nonlinear governing equations are obtained by Hamilton principle and dispersed by differential quadrature (DQ) method. The

Newmark- β method associated with Newton–Raphson iterative process is adopted to parametrically identify the impact force and the dynamic response of the system. The effects of geometric imperfection, weight fraction and distribution pattern of GPLs, temperature variation, thickness of piezoelectric layer and impactor's initial velocity on nonlinear low-velocity impact behaviors of geometrically imperfect GRC beams are discussed in detail. Our results illustrate that the coupling effect of geometric imperfection and thermo-electro-mechanical load has a significant effect on the nonlinear low-velocity impact behavior of GRC beam, and GPLs distributing into the piezoelectric layers is better for reducing the impact response of geometrically imperfect GRC piezoelectric beam.

Keywords Low-velocity impact · Thermo-electro-mechanical load · Graphene nanoplatelets · Geometric imperfection · Nonlinear Hertz contact law · Functionally graded materials

W. Zhang · L.-J. Guo · Y. Wang · J.-J. Mao (✉) · J. Yan
Beijing Key Laboratory of Nonlinear Vibrations and Strength of Mechanical Structures, Faculty of Materials and Manufacturing, Beijing University of Technology, Beijing 100124, People's Republic of China
e-mail: jjjia.mao@bjut.edu.cn

J. Yan
Engineering Research and Development Centre for Underground Technology of Jiangxi Province, School of Civil Engineering and Architecture, East China Jiaotong University, Nanchang 330013, Jiangxi, People's Republic of China

1 Introduction

Geometric imperfections are inevitable in engineering structures due to the influence of manufacturing and environmental factors, and these imperfections have significant effects on the mechanical behaviors of

structures [1–3], especially for the vibration, buckling and nonlinear dynamic behaviors [4–6]. Sheinman et al. [6] studied the imperfection sensitivity of an isotropic beam under a nonlinear elastic foundation. Farokhi et al. [7] investigated the effect of geometric imperfection on the nonlinear resonance of the Timoshenko microbeam. Wadee [8] proposed the one-dimensional imperfection model to simulate various global and localized imperfections existing in engineering structure, and then conducted a detailed research on buckling and post-buckling behaviors of the geometrically imperfect sandwich panel. Their results shown that the mechanical behaviors of structures are very sensitive to the geometric imperfections. Obviously, the research on the dynamic behaviors of structures with geometric imperfections is of great significance in engineering design.

Except the isotropic homogeneous structures mentioned above, more and more lightweight and high strength materials and high-performance composite structures are emerging in the field of aerospace and engineering applications, such as the functionally graded materials (FGM), fiber-reinforced composite structures and carbon-based composite structures [9–12]. In the framework of isogeometric analysis [13], Nguyen and his co-workers calculated the static and dynamic behaviors of the high-performance composite structures, such as the vibration of FGM piezoelectric porous microplates [14] and postbuckling of functionally graded carbon nanotube-reinforced composite (CNTRC) shells [15]. When the high-performance composite structures operate under thermo-electro-mechanical loads, their mechanical behaviors can significantly be affected by their working conditions. Yang and his co-authors [16, 17] analyzed the large amplitude vibration and thermal bifurcation buckling of carbon nanotube-reinforced composite (CNTRC) beams bonded with piezoelectric layers. Liew's group [18, 19] researched active vibration control of FG composite plates bonded with the piezoelectric actuator and sensor. Wu et al. [20, 21] analyzed the post-buckling and free vibration of FG-CNTRC beam with geometric imperfections under thermal–mechanical–electrical loads.

Recently, graphene nanoplatelets (GPLs) have shown tremendous potentials in the development of high-performance composites due to its unique mechanical properties since its first report by Novoselov et al. [22]. Extensive theoretical and

experimental investigations have shown that the dispersion of GPLs in the polymer matrix can significantly improve its mechanical properties [23–25]. Yang's group firstly proposed the functionally graded (FG) GPLs-reinforced composite (GRC) structures and carried out a detailed study on their bending, buckling and vibration behaviors [26–29]. Mao et al. [30–33] conducted a detailed analysis of the static and dynamic behaviors of FG-GRC structures. Rahimi et al. [34, 35] employed a semi-analytical solution to obtain the three-dimensional bending and free vibration behaviors of FG-GRC cylindrical shells. Furthermore, many scholars have studied the vibrations and stability of FG-GRC structures under various loads, including transverse excitation [36, 37], axial compression [38], thermal loads [39] and impact loads [40]. Results illustrated that the GPL reinforcements can significantly enhance the stiffness of the GRC structures, and the enhancement effect largely depends on the distribution pattern of GPLs in matrix.

According to the researches about nonlinear behaviors of FG-GRC structures with geometric imperfections, shapes and amplitudes of geometric imperfections have significant effects on the buckling [41, 42], nonlinear vibration [4, 43] and resonance [44] of FG-GRC structures. It is worth noting that impact is one of common loads for engineering structures, which may result in internal damage and even lead to severe failure of structures. Introducing the modified Hertz model, Fan et al. [45, 46] discussed the low-velocity impact response of FG-GRC structures resting on visco-elastic foundations. Based on the energy-balance and spring-mass model, Dong et al. [47] predicted the low-velocity impact response of FG-GRC cylindrical shells under axial load and thermal loads. Selim et al. [48] examined the impact behaviors of FG-GRC plates resting on Winkler-Pasternak elastic foundations by using a meshless approach.

The existing literature have researched the low-velocity impact behaviors of intact GRC structures and the nonlinear dynamic behaviors of geometrically imperfect GRC structures in detail separately. To our best knowledge, there is no relevant reports on the impact behavior of GRC beam with geometric imperfections. But it is the utmost important for the safety and longevity of engineering structures, especially for the high-performance composite structures working under complex loading, such as the situation among thermal, electrical and mechanical loads.

In order to investigate the couple effect of the low-velocity impact and geometric imperfections on the nonlinear dynamic behaviors of the GRC beam subjected to thermal–mechanical–electrical loads, the present work introduces a theoretical model and numerical analysis method. For the geometric imperfect GRC beam with surface-bonded piezoelectric layers subjected to low-velocity impact and thermo-electro-mechanical loads, the governing equations of motion are derived based on the first-order shear deformation theory, von Kármán nonlinear displacement–strain relationship and Hamilton’s principle, and dispersed by differential quadrature (DQ) method. The Newmark- β method associated with Newton–Raphson iterative method is employed to study the effects of the weight fraction and distribution pattern of GPLs, the types and amplitude of geometric imperfections, temperature variation, impact velocity, as well as thickness of the piezoelectric layer on impact force and impact response of the geometrically imperfect GRC piezoelectric beam.

2 Theoretical models

2.1 Geometry model

Figure 1a illustrates a GRC beam with geometric imperfection. The length, width and thickness of the GRC beam are L , b and h , respectively. Two piezoelectric layers with a thickness of h_p are perfectly bonded on the upper and lower surfaces of the

geometrically imperfect GRC beam and respectively applied with voltage U_0 . The hinged supported boundary conditions are considered. The GRC beam is subjected a uniform temperature variation $\Delta T = T - T_0$ and it is stress-free at initial temperature T_0 . It is assumed that the material properties of GRC beam are independent of the varying temperatures to focus on the coupled effect of the temperature variation and geometric imperfection on the nonlinear low-velocity impact response of the GRC piezoelectric beam. The geometrically imperfect GRC piezoelectric beam is impacted by a spherical impactor with initial velocity V_0 . m_i and R_i respectively denote the mass and radius of the impactor.

The geometric imperfection $w^*(x)$ is simulated in the form of the product of the trigonometric and hyperbolic functions [8]

$$w^*(x) = A_0 h \operatorname{sech}[a(x/L - c)] \cos[b\pi(x/L - c)]. \quad (1)$$

where a is a constant, representing the localization degree of the imperfection, and A_0 is the dimensionless amplitude of the geometric imperfection. The spherical impactor impacts to the concave surface of the GRC beam for $A_0 > 0$, as shown in Fig. 1, and the convex surface is impacted for $A_0 < 0$. Note that $w^*(x)$ is symmetric about $x/L = c$, and b is the half-wave numbers of the imperfection in x -axis. Sine, global (G) and localized (L) imperfections are considered. As presented in Fig. 2, the varying values of constants a , b and c represent various geometric imperfections, Sine, G_s and L_s ($s = 1, 2, 3, 4$).

Fig. 1 Structural schematic: **a** A model of an N -layered geometrically imperfect GRC piezoelectric beam subjected to low-velocity impact, **b** GPLs distribution patterns: UD, FG-X, FG-O

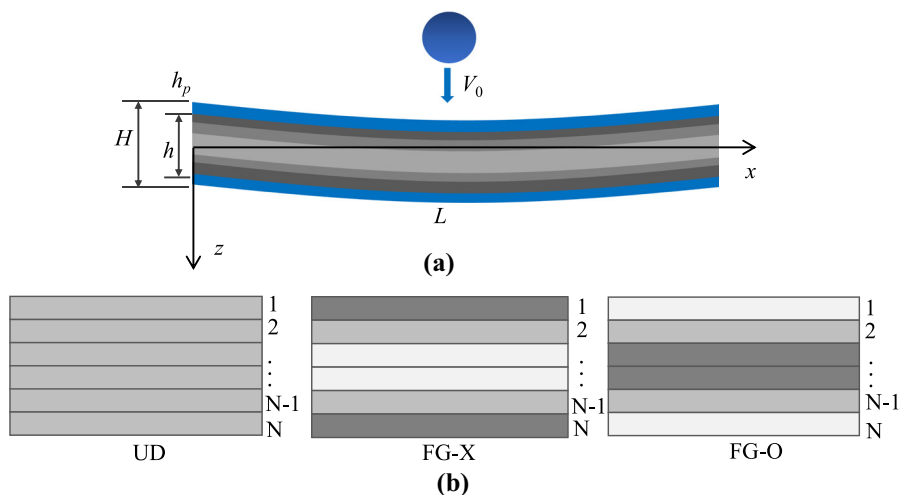
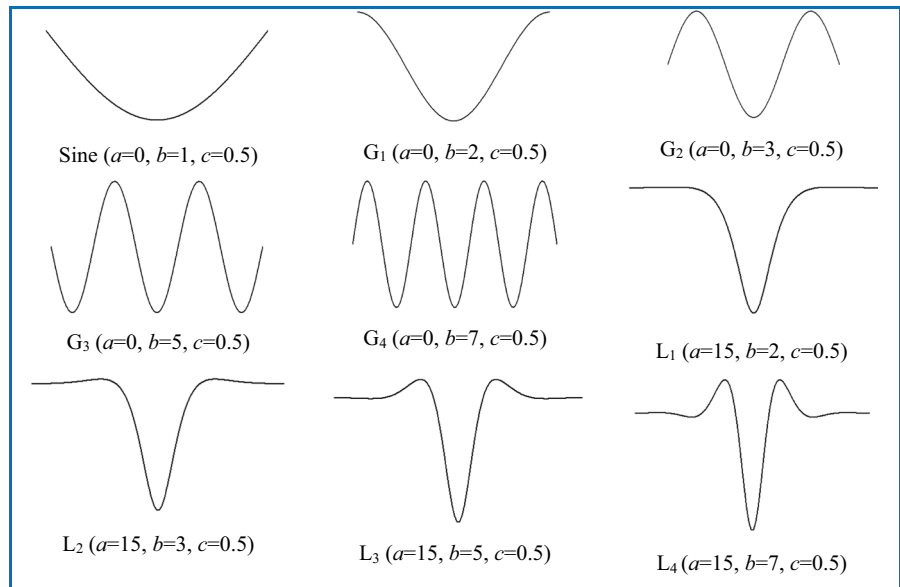


Fig. 2 Geometric imperfection modes



2.2 Nonlinear Hertz model

Based on Newton’s second law, the governing equation of motion for the impactor can be expressed as

$$m_i \ddot{y}_i(t) + F_C(t) = 0, \tag{2}$$

where $y_i(t)$ is the displacement of the impactor, and $F_C(t)$ is the impact force between the impactor and the impacted geometrically imperfect GRC piezoelectric beam.

When the contact area between the impactor and the impacted beam is much smaller than the geometries of the beam, Hertz contact theory can be utilized to calculate the impact force. The nonlinear low-velocity impact process can be divided into two phases, namely, loading phase and unloading phase [46, 49]. The loading phase starts from the moment that the impactor impacts to the target beam, and ends when the local contact indentation reaches to the maximum. The unloading phase begins at the local contact indentation reaching to the maximum, until the impactor totally departing from the geometrically imperfect GRC piezoelectric beam. According to the modified nonlinear Hertz contact proposed by Yang and Sun [50], the varying impact force $F_C(t)$ during these two different phases can be predicted through two different equations.

During the loading phase [49],

$$F_C(t) = K_C \alpha^{3/2}(t), \tag{3}$$

with the contact stiffness K_C and the local contact indentation $\alpha(t)$

$$K_C = \frac{4}{3} \sqrt{R_i} \left(\frac{1 - \nu_i^2}{Y_i} + \frac{1 - \nu_i^2}{Y_i} \right)^{-1}, \alpha(t) = y_i(t) - w_C(t) \tag{4}$$

where Y and ν are the Young’s modulus and Poisson ratio, respectively, and the subscript “ i ” and “ \bar{i} ” respectively represent the impactor and the top surface of the geometrically imperfect GRC piezoelectric beam. Besides, w_C denotes the deflection of the geometrically imperfect GRC piezoelectric beam at the impacted point.

During the unloading phase [49],

$$F_C(t) = F_{\max} \left(\frac{\alpha(t) - \alpha_0}{\alpha_{\max} - \alpha_0} \right)^{5/2}, \tag{5}$$

where α_{\max} and F_{\max} are respectively the maximum local contact indentation and the corresponding impact force, and α_0 is the permanent indentation of the target beam. If the plastic deformation is not considered, $\alpha_0 = 0$.

2.3 Physical parameter model

It is assumed that the GRC beam is composed by a mixture of an isotropic matrix and GPLs with length l_G , width w_G and thickness h_G . GPLs disperse into the GRC beam along its thickness direction. Both uniformly distributed (UD) and functionally graded (FG) patterns are taken into consideration, as shown in Fig. 1(b), namely UD, FG-X and FG-O. GPL volume fraction respectively decreases and increases in FG-X and FG-O from the top and bottom layers to the middle layers. In other words, the GPL volume fractions of the middle layers are the lowest in FG-X, but the GPL volume fractions of the middle layers are the highest in FG-O. GPL volume fraction $V_G^{(k)}$ in the k th layer of the GRC beam can be expressed as

$$U : V_G^{(k)} = V_G^* \tag{6}$$

$$FG - X : V_G^{(k)} = 2V_G^*(2k - N - 1)/N, \tag{7}$$

$$FG - O : V_G^{(k)} = 2V_G^*(1 - |2k - N - 1|)/N, \tag{8}$$

where

$$V_G^* = \frac{f_G}{f_G + (\rho_G/\rho_M)(1 - f_G)}. \tag{9}$$

f_G denotes the total GPL weight fraction. ρ_G and ρ_M are respectively the mass density of the GPLs and matrix, and $k = 1, 2, \dots, N$.

According to the Halpin-Tsai model [24] and the rule of mixture, the effective material properties, including Young's modulus $Y_C^{(k)}$, Poisson ratio $v_C^{(k)}$, mass density $\rho_C^{(k)}$ and thermal expansion coefficient $\alpha_C^{(k)}$ of the k th GRC layer, can be predicted by

$$Y_C^{(k)} = \frac{3\left(1 + 2\zeta_{LW}\zeta_{WH}\eta_L V_G^{(k)}\right)}{8\left(1 - \eta_L V_G^{(k)}\right)} \times Y_M + \frac{5\left(1 + 2\zeta_{WH}\eta_W V_G^{(k)}\right)}{8\left(1 + \eta_W V_G^{(k)}\right)} \times Y_M, \tag{10}$$

$$\rho_C^{(k)} = \rho_G V_G^{(k)} + \rho_M \left(1 - V_G^{(k)}\right), \tag{11}$$

$$v_C^{(k)} = v_G V_G^{(k)} + v_M \left(1 - V_G^{(k)}\right), \tag{12}$$

$$\alpha_C^{(k)} = \alpha_G V_G^{(k)} + \alpha_M \left(1 - V_G^{(k)}\right), \tag{13}$$

with

$$\eta_L = \frac{Y_G/Y_M - 1}{Y_G/Y_M + 2\zeta_{LW}\zeta_{WH}}, \eta_W = \frac{Y_G/Y_M - 1}{Y_G/Y_M + 2\zeta_{WH}}, \tag{14}$$

where the subscripts “ M ” and “ G ” represent matrix and GPLs, respectively. ζ_{LW} and ζ_{WH} are respectively the length-to-width ratio and width-to-thickness ratio of the GPLs, expressed by

$$\zeta_{LW} = \frac{l_G}{w_G}, \zeta_{WH} = \frac{w_G}{h_G}. \tag{15}$$

3 Nonlinear dynamic equations

In this study, the first-order shear deformation theory is used to estimate the deformation of the geometrically imperfect GRC piezoelectric beam. The axial and transverse displacements $\tilde{u}(x, z, t)$ and $\tilde{w}(x, z, t)$ of the novel beam can be presented by its mid-plane axial, transverse and rotary displacements $u(x, t)$, $w(x, t)$ and $\varphi(x, t)$, combined with the initial transverse geometric imperfection $w^*(x)$

$$\begin{aligned} \tilde{u}(x, z, t) &= u(x, t) + z\varphi(x, t), \\ \tilde{w}(x, z, t) &= w(x, t) + w^*(x). \end{aligned} \tag{16}$$

Referring to von Kármán nonlinear displacement-strain relationship, the normal strain ε_{xx} and shear strain γ_{xz} of the geometrically imperfect GRC piezoelectric beam are gained as

$$\varepsilon_{xx} = \frac{\partial u}{\partial x} + \frac{1}{2} \left(\frac{\partial w}{\partial x}\right)^2 + z \frac{\partial \varphi}{\partial x} + \frac{\partial w}{\partial x} \frac{dw^*}{dx}, \gamma_{xz} = \frac{\partial w}{\partial x} + \varphi. \tag{17}$$

The linear constitutive relations for the k th GRC layer and piezoelectric layers can be expressed as

$$\sigma_{xx}^{(k)} = Q_{11}^{(k)} \left(\varepsilon_{xx} - \alpha_C^{(k)} \Delta T\right), \tau_{xz}^{(k)} = Q_{55}^{(k)} \gamma_{xz}, \tag{18}$$

$$\begin{aligned} \sigma_{xx}^p &= Q_{11}^p (\varepsilon_{xx} - \alpha_p \Delta T) - e_{31} E_z, \tau_{xz}^p = Q_{55}^p \left(\frac{\partial w}{\partial x} + \varphi\right), \\ D_z &= e_{31} \varepsilon_{xx} + k_{33} E_z, \end{aligned} \tag{19}$$

where

$$Q_{11}^{(k)} = \frac{Y_C^{(k)}}{1 - \nu_C^{(k)2}}, Q_{55}^{(k)} = \frac{Y_C^{(k)}}{2(1 + \nu_C^{(k)})}, \tag{20}$$

$$Q_{11}^P = \frac{Y_P}{1 - \nu_P^2}, Q_{55}^P = \frac{Y_P}{2(1 + \nu_P)} \tag{21}$$

Y_P and ν_P are Young’s modulus and Poisson ratio of the piezoelectric layer, respectively, e_{31} , k_{33} and D_Z are respectively the piezoelectric stress constant, permittivity constant and electric displacement of the piezoelectric layer. The electric potential variation is considered to be linear throughout the thickness of piezoelectric layer as Ref. [51], so the electric field E_Z can be expressed as

$$E_Z = \frac{U_0}{h_P}. \tag{22}$$

Based on Hamilton principle, the partial differential governing equations of motion for geometrically imperfect GRC piezoelectric beam under low-velocity impact are obtained as

$$\frac{\partial N_x}{\partial x} = I_1 \frac{\partial^2 u}{\partial t^2} + I_2 \frac{\partial^2 \varphi}{\partial t^2}, \tag{23}$$

$$\begin{aligned} \frac{\partial}{\partial x} \left(N_x \frac{\partial w}{\partial x} + N_x \frac{\partial w^*}{\partial x} \right) + \frac{\partial Q}{\partial x} + F_C(t)\delta(x - x_C) \\ = I_1 \frac{\partial^2 w}{\partial t^2}, \end{aligned} \tag{24}$$

$$\frac{\partial M_x}{\partial x} - k_s Q_x = I_2 \frac{\partial^2 w}{\partial t^2} + I_3 \frac{\partial^2 \varphi}{\partial t^2}, \tag{25}$$

where the shear correction factor $k_s = 5/6$ and x_C is the location of the impacted point. I_j ($j = 1, 2$ and 3) are the inertia related terms

$$\begin{aligned} \begin{pmatrix} I_1 \\ I_2 \\ I_3 \end{pmatrix} = \sum_{k=1}^N \int_{h/2-k\Delta h}^{h/2-(k-1)\Delta h} \rho_C^{(k)} \begin{pmatrix} 1 \\ z \\ z^2 \end{pmatrix} dz \\ + \int_{-H/2}^{-h/2} \rho^P \begin{pmatrix} 1 \\ z \\ z^2 \end{pmatrix} dz \\ + \int_{h/2}^{H/2} \rho^P \begin{pmatrix} 1 \\ z \\ z^2 \end{pmatrix} dz. \end{aligned} \tag{26}$$

The in-plane force N_x , bending moment M_x and shear forces Q_x are respectively expressed by

$$\begin{aligned} N_x = A_{11} \left[\frac{\partial u}{\partial x} + \frac{1}{2} \left(\frac{\partial w}{\partial x} \right)^2 + \frac{\partial w}{\partial x} \frac{\partial w^*}{\partial x} \right] + B_{11} \frac{\partial \varphi}{\partial x} - N_x^P \\ - N_x^T, \end{aligned} \tag{27}$$

$$\begin{aligned} M_x = B_{11} \left[\frac{\partial u}{\partial x} + \frac{1}{2} \left(\frac{\partial w}{\partial x} \right)^2 + \frac{\partial w}{\partial x} \frac{\partial w^*}{\partial x} \right] + D_{11} \frac{\partial \varphi}{\partial x} - M_x^P \\ - M_x^T, \end{aligned} \tag{28}$$

$$Q_x = A_{55} \left(\frac{\partial u}{\partial x} + \varphi \right). \tag{29}$$

where the stiffness components A_{11} , B_{11} , D_{11} and A_{55} are respectively given by

$$\begin{aligned} \begin{pmatrix} A_{11} \\ B_{11} \\ D_{11} \end{pmatrix} = \sum_{k=1}^N \int_{h/2-k\Delta h}^{h/2-(k-1)\Delta h} Q_{11}^{(k)} \begin{pmatrix} 1 \\ z \\ z^2 \end{pmatrix} dz \\ + \int_{-H/2}^{-h/2} Q_{11}^P \begin{pmatrix} 1 \\ z \\ z^2 \end{pmatrix} dz \\ + \int_{h/2}^{H/2} Q_{11}^P \begin{pmatrix} 1 \\ z \\ z^2 \end{pmatrix} dz, \end{aligned} \tag{30}$$

$$\begin{aligned} A_{55} = \sum_{k=1}^N \int_{h/2-k\Delta h}^{h/2-(k-1)\Delta h} Q_{55}^{(k)} k_s dz + \int_{-H/2}^{-h/2} Q_{55}^P k_s dz \\ + \int_{h/2}^{H/2} Q_{55}^P k_s dz. \end{aligned} \tag{31}$$

The thermal and electric related loads are written as

$$\begin{aligned} \begin{pmatrix} N_x^T \\ M_x^T \end{pmatrix} = \sum_{k=1}^N \int_{h/2-k\Delta h}^{h/2-(k-1)\Delta h} Q_{11}^{(k)} \alpha_c^{(k)} \begin{pmatrix} 1 \\ z \end{pmatrix} dz \\ + \int_{-H/2}^{-h/2} Q_{11}^P \alpha_P \begin{pmatrix} 1 \\ z \end{pmatrix} dz \\ + \int_{h/2}^{H/2} Q_{11}^P \alpha_P \begin{pmatrix} 1 \\ z \end{pmatrix} dz, \end{aligned} \tag{32}$$

$$\begin{aligned} \begin{pmatrix} N_x^P \\ M_x^P \end{pmatrix} = \int_{-H/2}^{-h/2} e_{31} E_Z \begin{pmatrix} 1 \\ z \end{pmatrix} dz \\ + \int_{h/2}^{H/2} e_{31} E_Z \begin{pmatrix} 1 \\ z \end{pmatrix} dz, \end{aligned} \tag{33}$$

Obviously, $M_x^P = 0$. In this study, the geometrically imperfect GRC piezoelectric beam has hinged supported boundary conditions at both ends ($x = 0, L$). The corresponding boundary conditions are given as follows

$$u = 0, w = 0, M_x = 0 \tag{34}$$

Introducing the following dimensionless quantities

$$\begin{aligned} & a_{11} \left[\frac{\partial^2 U}{\partial X^2} + \frac{1}{\eta} \frac{\partial^2 W}{\partial X^2} \left(\frac{\partial W}{\partial X} + \frac{dW^*}{dX} \right) + \frac{1}{\eta} \frac{\partial W}{\partial X} \frac{d^2 W^*}{dX^2} \right] \\ & + b_{11} \frac{\partial^2 \psi}{\partial X^2} \\ & = \tilde{I}_1 \frac{\partial^2 U}{\partial \tau^2} + \tilde{I}_2 \frac{\partial^2 \psi}{\partial \tau^2} \end{aligned} \tag{36}$$

$$\begin{aligned} & \left[a_{11} \left(\frac{1}{\eta} \frac{\partial^2 U}{\partial X^2} + \frac{1}{\eta^2} \frac{\partial^2 W}{\partial X^2} \frac{\partial W}{\partial X} + \frac{1}{\eta^2} \frac{\partial^2 W}{\partial X^2} \frac{dW^*}{dX} + \frac{1}{\eta^2} \frac{\partial W}{\partial X} \frac{d^2 W^*}{dX^2} \right) + \frac{b_{11}}{\eta} \frac{\partial^2 \psi}{\partial X^2} \right] \left(\frac{\partial W}{\partial X} + \frac{dW^*}{dX} \right) \\ & + \left\{ a_{11} \left[\frac{1}{\eta} \frac{\partial U}{\partial X} + \frac{1}{2\eta^2} \left(\frac{\partial W}{\partial X} \right)^2 + \frac{1}{\eta^2} \frac{\partial W}{\partial X} \frac{dW^*}{dX} \right] + \frac{b_{11}}{\eta} \frac{\partial \psi}{\partial X} - \tilde{N}_x^T - \tilde{N}_x^P \right\} \left(\frac{\partial^2 W}{\partial X^2} + \frac{d^2 W^*}{dX^2} \right) \\ & + a_{55} \left(\frac{\partial^2 W}{\partial X^2} + \eta \frac{\partial \psi}{\partial X} \right) + F_C^*(t) \delta(X - X_C) = \tilde{I}_1 \frac{\partial^2 W}{\partial \tau^2} \end{aligned} \tag{37}$$

$$b_{11} \left[\frac{\partial^2 U}{\partial X^2} + \frac{1}{\eta} \frac{\partial W}{\partial X} \frac{\partial^2 W}{\partial X^2} + \frac{1}{\eta} \frac{\partial^2 W}{\partial X^2} \frac{dW^*}{dX} + \frac{1}{\eta} \frac{\partial W}{\partial X} \frac{d^2 W^*}{dX^2} \right] + d_{11} \frac{\partial^2 \psi}{\partial X^2} - a_{55} \left(\eta \frac{\partial W}{\partial X} + \eta^2 \psi \right) = \tilde{I}_2 \frac{\partial^2 U}{\partial \tau^2} + \tilde{I}_3 \frac{\partial^2 \psi}{\partial \tau^2}. \tag{38}$$

$$\begin{aligned} X &= \frac{x}{L}, (U, W, W^*) = \frac{(u, w, w^*)}{h}, \psi = \varphi, \eta = \frac{L}{h}, \\ \tau &= \frac{t}{L} \sqrt{\frac{A_{110}}{I_{10}}}, \\ (a_{11}, a_{55}, b_{11}, d_{11}) &= \left(\frac{A_{11}}{A_{110}}, \frac{A_{55}}{A_{110}}, \frac{B_{11}}{A_{110}h}, \frac{D_{11}}{A_{110}h^2} \right), \\ (\tilde{I}_1, \tilde{I}_2, \tilde{I}_3) &= \left(\frac{I_1}{I_{10}}, \frac{I_2}{I_{10}h}, \frac{I_3}{I_{10}h^2} \right), \\ (\tilde{N}^P, \tilde{N}^T) &= \left(\frac{N^P, N^T}{A_{110}}, F_C^* = \frac{F_C L}{A_{110}h}, \right. \\ A_{110} &= \frac{Y_M}{1 - \nu_M^2} h, I_{10} = \rho_M h, \end{aligned} \tag{35}$$

The partial differential governing Eqs. (23)–(25) can be rewritten in the dimensionless forms

4 Solution procedure

In this paper, the differential quadrature (DQ) method [32, 52] and Newmark-β method [53] combined with Newton–Raphson iterative process [13, 54] are introduced to numerically analyze the nonlinear low-velocity impact response of the geometrically imperfect GRC piezoelectric beam subjected to thermo-electro-mechanical loads. According to DQ method, the dimensionless displacement components U, W, ψ of the geometrically imperfect GRC piezoelectric beam and their r th derivatives with respect to X_i are approximated in following forms

$$\{U, W, \psi\} = \sum_{m=1}^n l_m(X) \{U_m, W_m, \psi_m\}, \tag{39}$$

$$\frac{\partial^r}{\partial X^r} \{U, W, \psi\} \Big|_{X=X_i} = \sum_{m=1}^n C_{im}^{(r)} \{U_m, W_m, \psi_m\}, \quad (40)$$

where $\{U_m, W_m, \psi_m\} = \{U, W, \psi\}|_{X=X_m}$, $l_m(X)$ is the Lagrange interpolation polynomial, $C_{im}^{(r)}$ is the weighting coefficients of the r th derivative at $X = X_i$, n is the total number of nodes distributed along the whole length of the GRC beam. In the present work, the distribution of nodes is given by the following equation

$$X_i = \frac{1}{2} \left[1 - \cos \frac{\pi(i-1)}{n-1} \right] \quad (i = 1, 2, \dots, n). \quad (41)$$

Substituting Eqs. (39) and (40) into Eqs. (36)–(38), the dimensionless partial differential governing equations for nonlinear low-velocity impact response of geometrically imperfect GRC piezoelectric beam can be written as following ordinary differential equations

$$a_{11} \sum_{m=1}^n C_{im}^{(2)} U_m + \frac{a_{11}}{\eta} \left[\sum_{m=1}^n C_{im}^{(1)} W_m \sum_{m=1}^n C_{im}^{(2)} W_m + \frac{dW^*}{dX} \Big|_{X=X_i} \sum_{m=1}^n C_{im}^{(2)} W_m + \frac{d^2 W^*}{dX^2} \Big|_{X=X_i} \sum_{m=1}^n C_{im}^{(1)} W_m \right] + b_{11} \sum_{m=1}^n C_{im}^{(2)} \psi_m = \tilde{I}_1 \ddot{U}_i + \tilde{I}_2 \ddot{\psi}_i \quad (42)$$

$$\begin{aligned} & \left[\frac{a_{11}}{\eta} \sum_{m=1}^n C_{im}^{(2)} U_m + \frac{a_{11}}{\eta^2} \left(\sum_{m=1}^n C_{im}^{(1)} W_m \sum_{m=1}^n C_{im}^{(2)} W_m + \frac{dW^*}{dX} \Big|_{X=X_i} \sum_{m=1}^n C_{im}^{(2)} W_m + \frac{d^2 W^*}{dX^2} \Big|_{X=X_i} \sum_{m=1}^n C_{im}^{(1)} W_m \right) \right. \\ & \quad \left. + \frac{b_{11}}{\eta} \sum_{m=1}^n C_{im}^{(2)} \psi_m \right] \left(\sum_{m=1}^n C_{im}^{(1)} W_m + \frac{dW^*}{dX} \Big|_{X=X_i} \right) + \left(\frac{a_{11}}{\eta} \sum_{m=1}^n C_{im}^{(1)} U_m + \frac{a_{11}}{\eta^2} \frac{dW^*}{dX} \Big|_{X=X_i} \sum_{m=1}^n C_{im}^{(1)} W_m \right. \\ & \quad \left. + \frac{a_{11}}{2\eta^2} \sum_{m=1}^n C_{im}^{(1)} W_m \sum_{m=1}^n C_{im}^{(1)} W_m + \frac{b_{11}}{\eta^2} \sum_{m=1}^n C_{im}^{(1)} \psi_m - \tilde{N}_x^T \Big|_{X=X_i} - \tilde{N}_x^P \Big|_{X=X_i} \right) \left(\sum_{m=1}^n C_{im}^{(2)} W_m + \frac{d^2 W^*}{dX^2} \Big|_{X=X_i} \right) \\ & \quad + a_{55} \left(\sum_{m=1}^n C_{im}^{(2)} W_m + \eta \sum_{m=1}^n C_{im}^{(1)} \psi_m \right) = \tilde{I}_1 \ddot{W}_i - F_C^*(\tau) \delta(X - X_C) \Big|_{X=X_i}, \end{aligned} \quad (43)$$

$$b_{11} \sum_{m=1}^n C_{im}^{(2)} U_m + \frac{b_{11}}{\eta} \left(\sum_{m=1}^n C_{im}^{(1)} W_m \sum_{m=1}^n C_{im}^{(2)} W_m + \frac{dW^*}{dX} \Big|_{X=X_i} \sum_{m=1}^n C_{im}^{(2)} W_m + \frac{d^2 W^*}{dX^2} \Big|_{X=X_i} \sum_{m=1}^n C_{im}^{(1)} W_m \right) + d_{11} \sum_{m=1}^n C_{im}^{(2)} \psi_m - a_{55} \left(\eta \sum_{m=1}^n C_{im}^{(1)} W_m + \eta^2 \psi_i \right) = \tilde{I}_2 \ddot{U}_i + \tilde{I}_3 \ddot{\psi}_i. \quad (44)$$

With the DQ method, the boundary conditions in Eq. (34) can be rewritten as

$$b_{11} \left[\sum_{m=1}^n C_{1m}^{(1)} U_m + \frac{1}{2\eta} \left(\sum_{m=1}^n C_{1m}^{(1)} W_m \right)^2 + \frac{1}{\eta} \frac{dW^*}{dX} \Big|_{X=X_1} \sum_{m=1}^n C_{1m}^{(1)} W_m \right] + d_{11} \sum_{m=1}^n C_{1m}^{(1)} \Psi_m - M_x^T \Big|_{X=X_1} = 0, U_1 = 0, W_1 = 0, \tag{45}$$

$$b_{11} \left[\sum_{m=1}^n C_{nm}^{(1)} U_m + \frac{1}{2\eta} \left(\sum_{m=1}^n C_{nm}^{(1)} W_m \right)^2 + \frac{1}{\eta} \frac{dW^*}{dx} \Big|_{X=X_n} \sum_{m=1}^n C_{nm}^{(1)} W_m \right] + d_{11} \sum_{m=1}^n C_{nm}^{(1)} \Psi_m - M_x^T \Big|_{X=X_n} = 0, U_n = 0, W_n = 0 \tag{46}$$

Hence, the above ordinary differential equations can be written as the following matrix equation

$$\mathbf{M}\ddot{\mathbf{d}} + (\mathbf{K}_L + \mathbf{K}_{NL})\mathbf{d} = \mathbf{F} + \mathbf{R}, \tag{47}$$

where $\mathbf{d} = \{ \{U_i\}^T, \{W_i\}^T, \{\psi_i\}^T \}^T$ is the unknown displacement vector, $i = 1 \dots n$. \mathbf{M} denotes the mass matrix, \mathbf{K}_L and \mathbf{K}_{NL} denote the structural linear and nonlinear stiffness matrix. Additionally, \mathbf{F} and \mathbf{R} are respectively time-dependent and time-independent load vectors, which respectively generated by impact and the geometrically imperfect combined with the thermo-electro-mechanical load

$$\mathbf{F} = \begin{pmatrix} \{0\}_{n \times 1} \\ \{F_C^*(\tau)\delta(X - X_C)|_{X=X_i}\}_{n \times 1} \\ \{0\}_{n \times 1} \end{pmatrix}, \tag{48}$$

$$\mathbf{R} = \begin{pmatrix} \{0\}_{n \times 1} \\ \left\{ (\tilde{N}_x^T + \tilde{N}_x^P) \frac{d^2 W^*}{dx^2} \Big|_{X=X_i} \right\}_{n \times 1} \\ \{0\}_{n \times 1} \end{pmatrix}.$$

Stiffness-proportional damping matrix $\mathbf{C} = (2\zeta/\omega_l)\mathbf{K}_L$ [55–57] is considered to model energy dissipation of the impacted geometrically imperfect GRC piezoelectric beam, Eq. (44) can be written as

$$\mathbf{M}\ddot{\mathbf{d}} + \mathbf{C}\dot{\mathbf{d}} + (\mathbf{K}_L + \mathbf{K}_{NL}(\mathbf{d}))\mathbf{d} = \mathbf{F} + \mathbf{R} \tag{49}$$

where ζ is modal damping factor, and ω_l is the corresponding natural frequency. In this paper, ω_l is taken as the first natural frequency.

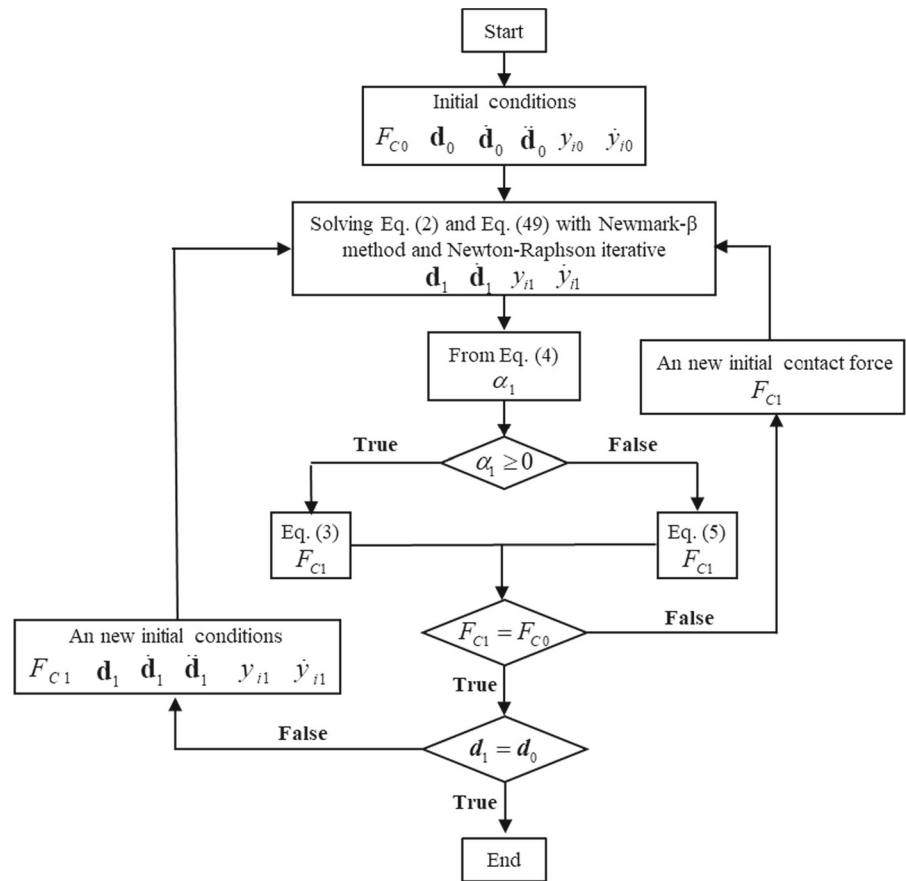
Assuming the initial conditions of the impactor as

$$y_i(0) = 0, \dot{y}_i(0) = V_0, \tag{50}$$

the governing equations of motion for the impactor, Eq. (2), and the ordinary differential equation of motion for the geometrically imperfect GRC piezoelectric beam, Eq. (49), can be solved parametrically by combining the Newmark- β method [53] with the Newton–Raphson iterative method [13, 54] to analyze the time-dependent impact force $F_C(t)$ and nonlinear dynamic behaviors of the low-velocity impact system. Figure 3 is the flowchart for the solution procedure, which is processing as below.

- i. For the first time-step, assuming an initial impact force F_{C0} , the displacements y_{i1} and \mathbf{d}_1 of the impactor and geometrically imperfect GRC piezoelectric beam can be respectively solved by Eq. (2) and Eq. (49) according to initial conditions $\mathbf{d}_0, \dot{\mathbf{d}}_0, \ddot{\mathbf{d}}_0, y_{i0}$ and \dot{y}_{i0} .
- ii. Applying the displacements obtained from step i into Eq. (3), a new impact force F_{C1} and local contact indentation can be predicted (Note that when the local contact indentation reaches the

Fig. 3 Flowchart for solving the nonlinear dynamic equations of geometrically imperfect GRC piezoelectric beams under low-velocity impact



maximum, the new impact force needs to be calculated by Eq. (5)). If F_{C1} is close to F_{C0} , turn to step iii. If not, take the new impact force F_{C1} as the initial impact force, and repeat step i.

- iii. Treating the displacements and impact force obtained from steps i and ii as the initial conditions for the next time-step, repeat steps i and ii.
- iv. When the central displacement of the geometrically imperfect GRC piezoelectric beam remains unchanged, the iterative process ends.

5 Results and discussions

In this section, the nonlinear low-velocity impact behaviors are analyzed numerically for the GRC beam with geometric imperfections under thermo-electro-mechanical loads. The effects of weight fraction f_G and distribution pattern of GPLs, mode and amplitude A_0

of imperfections, initial impact velocity V_0 , temperature variation ΔT and thickness ratio h_P/h on the impact force and dynamic response of the system are discussed in detailed.

Epoxy is selected as the matrix material of GRC beam, and the piezoelectric material is made by Polyvinylidene fluoride (PVDF). Material parameters [32, 33, 58] of epoxy, GPLs and PVDF are respectively

$$\text{Epoxy: } E_M = 3.0 \text{ GPa, } \rho_M = 1200 \text{ kg/m}^3, \nu_M = 0.34, \alpha_M = 60 \times 10^{-6} / \text{K}$$

$$\text{GPLs: } E_G = 1010 \text{ GPa, } \rho_G = 1060 \text{ kg/m}^3, \nu_M = 0.186, \alpha_G = 5 \times 10^{-6} / \text{K}$$

$$\text{PVDF: } E_P = 1.44 \text{ GPa, } \rho_P = 1929 \text{ kg/m}^3, \nu_P = 0.29, \alpha_P = 145 \times 10^{-6} / \text{K}, e_{31} = 0.05043 \text{ C/m}^2, k_{33} = 0.5957 \times 10^{-9} \text{ V/cm}$$

If there is no special instruction, length of the considered GRC beam $L = 50$ mm, thicknesses of GRC host beam and piezoelectric layers are respectively $h = 10$ mm and $h_p = 0.5$ mm, dimensionless amplitude of the geometric imperfection $A_0 = 0.02$, the applied piezoelectric actuator voltage $U_0 = 400$ V, temperature variation $\Delta T = 50$ K and damping factor $\zeta = 0.1$. The total number of the layers in the GRC host beam is $N = 12$. The geometric parameters of GPLs are $l_G \times w_G \times h_G = 2.5 \mu\text{m} \times 1.5 \mu\text{m} \times 1.5 \text{nm}$ and total weight fraction of GPLs is $f_G = 0.3\%$. The impactor is made of steel, and its material parameters are $Y_i = 207$ GPa, $\rho_i = 7960$ kg/m³ and $\nu_i = 0.3$. It is assumed that the impactor's radius is $R_i = 5$ mm, and the impactor

Table 1 Comparison results: Nonlinear frequency ratios of FG-X CNTRC beams with/without L₁-mode imperfection

W_{\max}	Intact		L ₁ -mode	
	Wu et al. [59]	Present	Wu et al. [59]	Present
0	1	1	1.0031	1.0020
0.1	1.0043	1.0045	1.0073	1.0126
0.2	1.0171	1.0180	1.0200	1.0319
0.3	1.0382	1.0400	1.0414	1.0594
0.4	1.0700	1.0700	1.0709	1.0947
0.5	1.1027	1.1073	1.1085	1.1371

with initial velocity $V_0 = 5$ m/s impacts on the center ($X_C = 0.5$) of the top surface for the geometrically imperfect GRC piezoelectric beam.

Convergence and comparison studies are firstly performed to ensure the effectiveness and accuracy of the present method. Figure 4 calculates and compares the effect of geometric imperfection modes on (a) the highest impact force and the (b) maximum central deflections of the geometrically imperfect GRC piezoelectric beams with varying nodes number n during the impact process. Obviously, L-mode imperfections converge slowly. It is because L-mode imperfections have sudden changes in geometric characteristics (Fig. 2). Even G₁-mode has the lowest impact force, it leads to the biggest center deflection. Hence, G₁-mode imperfection is the most harmful geometric imperfection for the stability of the GRC piezoelectric beam under impact. In the following

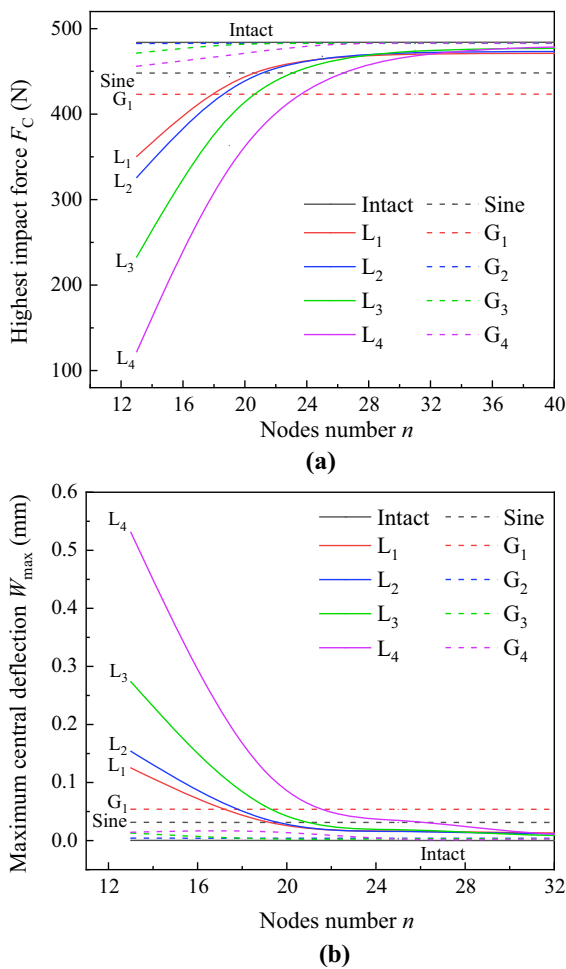


Fig. 4 Convergence results: the **a** highest impact force and **b** maximum central deflection of X-GRC piezoelectric beam with different geometric imperfections

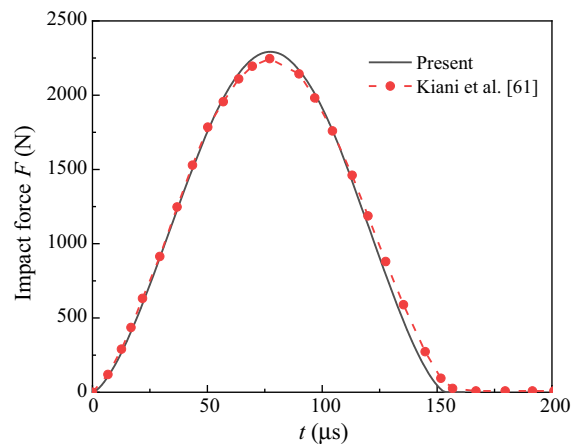


Fig. 5 Comparison of impact force history of the FG-X CNTRC beam under low-velocity impact load

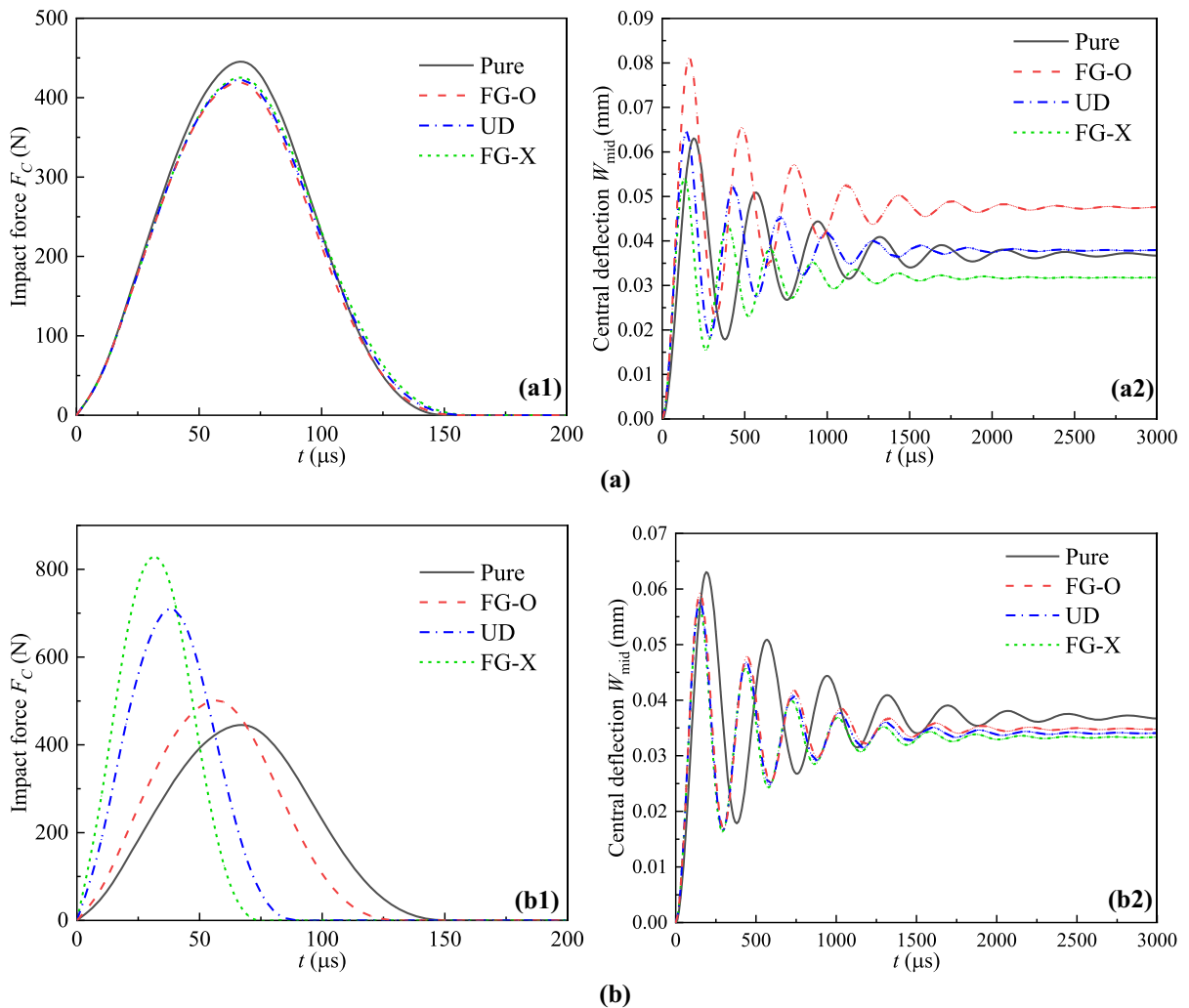


Fig. 6 Effect of GPL distribution patterns on the impact force and impact response of the geometrically imperfect GRC piezoelectric beam: **a** GPLs distributing into the GRC core beam and **b** GPLs distributing into the piezoelectric layers

analyses, we pay attention to the G_1 -mode imperfect GRC piezoelectric beam with nodes number $n = 13$.

The comparison results are given in Table 1 and Fig. 5. In Table 1, the nonlinear frequency ratios are compared with Wu et al.'s results [59] for the intact and L_1 -mode imperfect FG-X CNTRC beams with nodes number $n = 39$. Figure 5 compares the impact force history with Kiani et al.'s results [60] for the intact FG-X CNTRC beam subjected to a low-velocity impact with $V_0 = 3$ m/s. The comparison results show that our results are in good agreement with the existing literature results.

Figure 6 shows the influence of GPL distribution patterns (FG-X, UD, FG-O) on the impact force and

impact response of the geometrically imperfect GRC piezoelectric beam. The case of pure epoxy piezoelectric beam's results is also given for comparing. GPLs distributing into the GRC core beam and the piezoelectric layers are respectively considered in Fig. 6a, b. It is known that GPL reinforcements can largely improve the stiffness of the matrix. Keeping in mind that the dynamic displacement and impact force F_C are respectively closely related to the bending stiffness of the structure and contact stiffness of the impacted area. Therefore, when GPLs distribute into the GRC core beam, the varying GPL distribution pattern can significantly affect the dynamic behaviors, but has little effect on the impact force F_C . To the

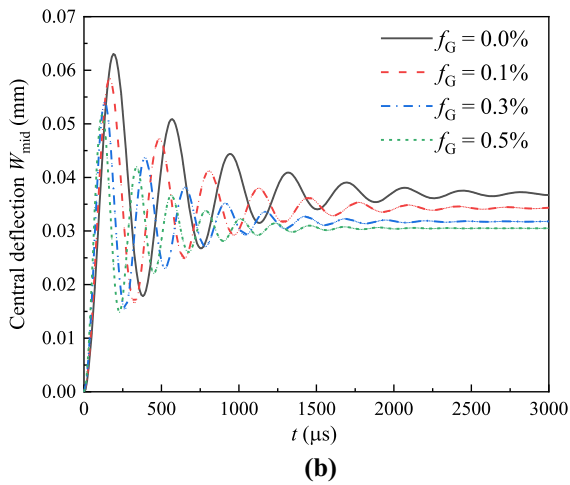
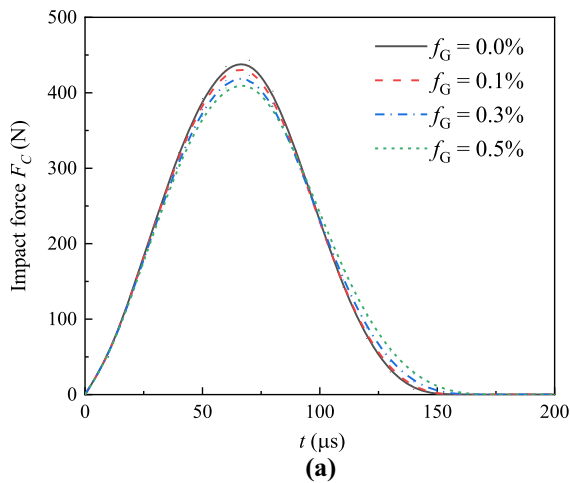


Fig. 7 Effect of GPL weight fractions on the **a** impact force and **b** impact response for X-GRC piezoelectric beams

contrary, the impact force is distinctly affected by the different GPL distribution pattern when GPLs distribute into the piezoelectric layers. In addition, the FG-X pattern has the lowest central deflection W_{mid} . For brief, only geometrically imperfect GRC piezoelectric beams with FG-X distributed GPLs are analyzed below.

Figure 7 illustrates the influence of GPL weight fractions ($f_G = 0.0\%$, 0.1% , 0.3% and 0.5%) on the (a) impact force history and (b) impact response of the geometrically imperfect FG-X GRC piezoelectric beams. $f_G = 0.0\%$ stands for the case of pure epoxy piezoelectric beam. As seen, both impact force F_C and central deflection W_{mid} decrease with the increase in GPL weight fractions, and the central deflection W_{mid} is more sensitive to the varying weight fraction of

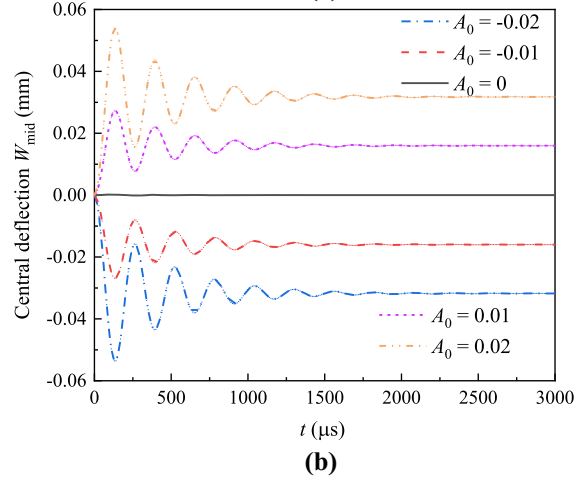
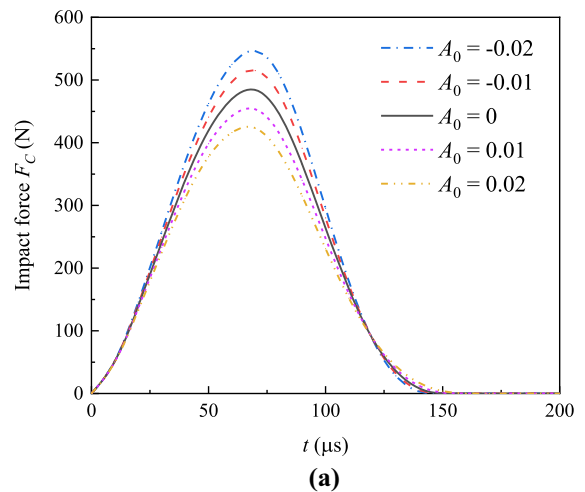


Fig. 8 Effect of imperfection amplitude on the **a** impact force and **b** impact response of the geometrically imperfect X-GRC piezoelectric beam

GPLs. It indicates that even a small amount of GPLs can contribute to a great increase in bending stiffness of the geometrically imperfect FG-X GRC piezoelectric beam.

Figure 8 displays the effect of the imperfection amplitude A_0 ($A_0 = -0.02, -0.01, 0, 0.01, 0.02$) on the (a) impact force and (b) impact response of the geometrically imperfect GRC piezoelectric beam. $A_0 = 0$ means the intact GRC piezoelectric beam. As seen, the impact force for the convex surface ($A_0 < 0$) of the GRC beam impacted is obviously greater than that for the concave surface ($A_0 > 0$) impacted. What's more, the impact force decreases with the increasing imperfection amplitude A_0 of the imperfection. Obviously, the final equilibrium position of

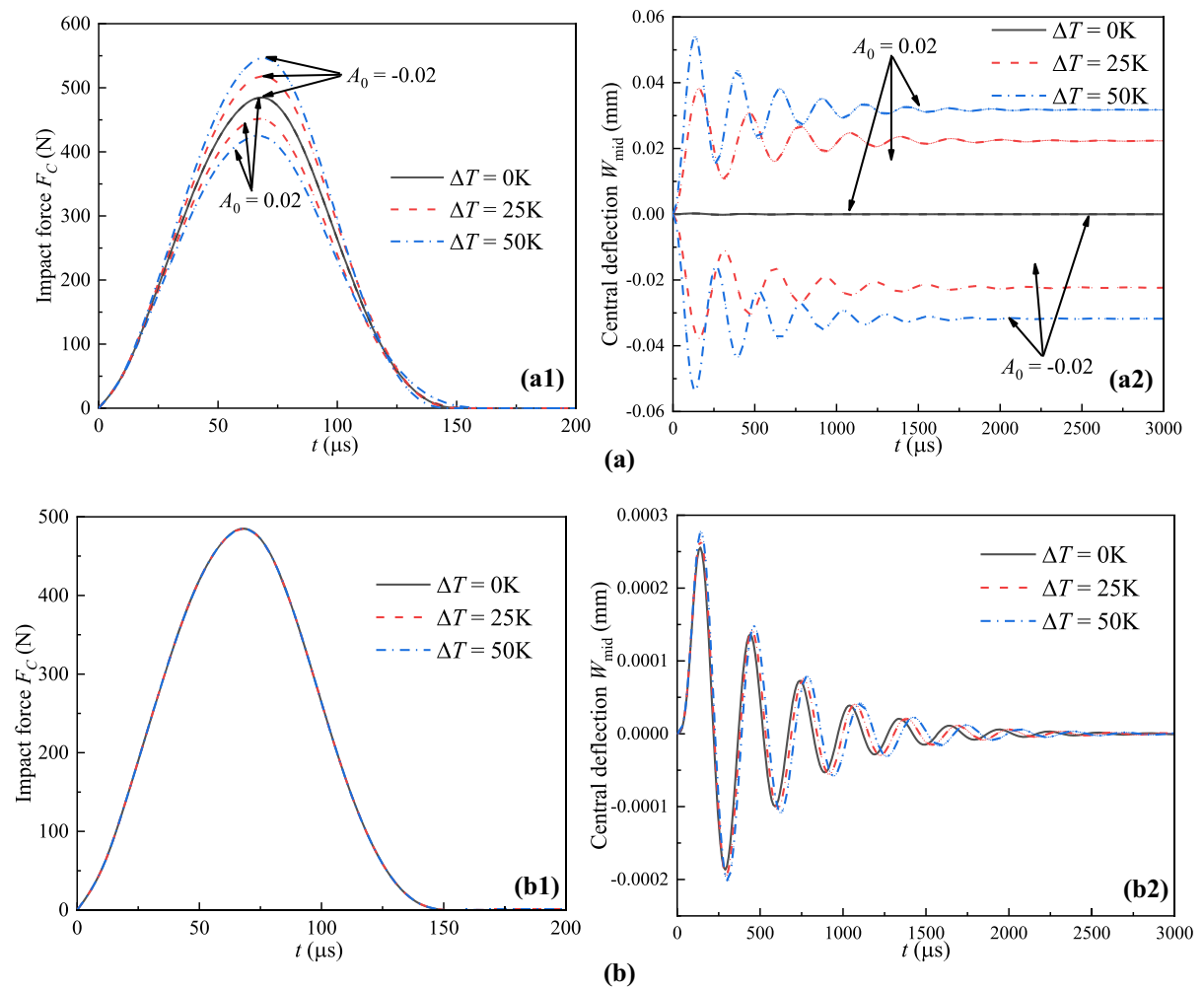


Fig. 9 Effect of temperature variation on the impact force and impact response of the **a** geometrically imperfect and **b** intact X-GRC piezoelectric beam

the geometrically imperfect GRC piezoelectric beam is also related to the sign of the imperfection amplitude A_0 . Bigger the absolute value of the imperfection amplitude is, further the final equilibrium position is apart from the z -axis. It is led by the direction and value of the component along z -axis of the force vector \mathbf{R} in Eq. (49).

Note that the force vector \mathbf{R} generated by the geometrically imperfect and the thermo-electro-mechanical load. $\mathbf{R} = \mathbf{0}$ when the GRC piezoelectric beam is intact.

To illustrate the coupled effect of the geometric imperfection and thermo-electro-mechanical load on the nonlinear low-velocity impact behavior, Fig. 9 shows the effect of temperature variation ($\Delta T = 0$ K,

25 K, 50 K) on the nonlinear low-velocity impact response of (a) geometrically imperfect ($A_0 = -0.02$ and 0.02) and (b) intact ($A_0 = 0$) GRC piezoelectric beams. It can be observed that the impact force and impact response of the imperfect cases are much more sensitive to the varying temperature than those of the intact one. In other words, the influence of thermal load on the nonlinear low-velocity impact response is barely for the intact GRC piezoelectric beam, but can be largely amplified once the geometric imperfection appearing.

Figure 10 demonstrates the (a) impact force history and (b) impact response of geometrically imperfect GRC piezoelectric beam impacted by different initial impactor velocities ($V_0 = 3$ m/s, 5 m/s and 7 m/s). As

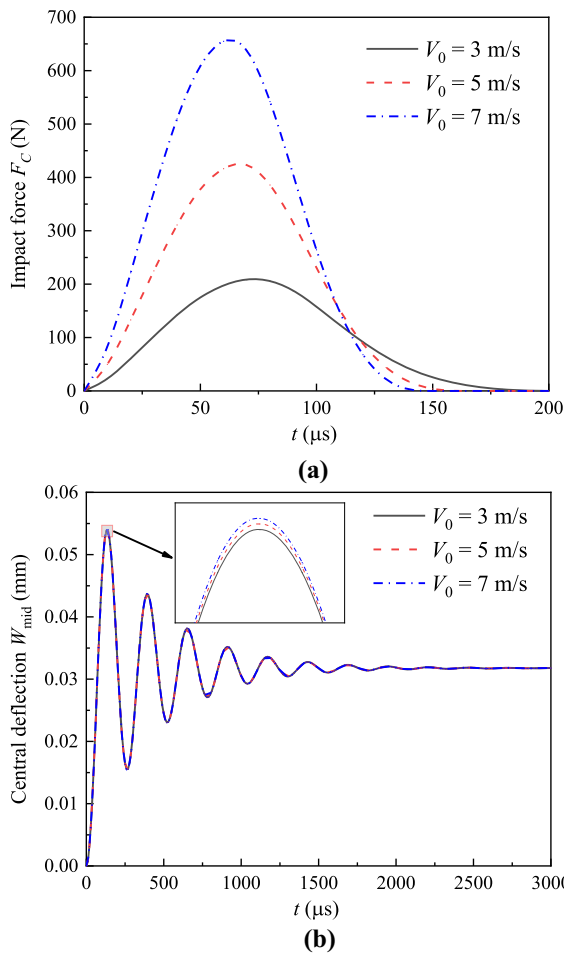


Fig. 10 Effect of initial indenter velocity on the **a** impact force and **b** impact response of the geometrically imperfect X-GRC piezoelectric beam

seen that the increase in the initial impactor velocity V_0 leads to the remarkably increase in the maximum impact force, but obviously decreases the impacted time. Besides, the maximum center displacement increases a little for the increasing initial impactor velocity, which accompany with an increasing initial energy.

Figure 11 demonstrates the effect of the thickness ratio ($h_p/h = 0, 1/10, 1/5$) of piezoelectric layer to GRC host beam on the (a) impact force F_C and (b) central deflection W_{mid} for the geometrically imperfect GRC piezoelectric beam. Here, we keep the thickness of GRC host beam unchanged. $h_p/h = 0$ represents GRC beam without any piezoelectric layers. Because the increase in piezoelectric layer thickness can improve the stiffness of the GRC piezoelectric beam,

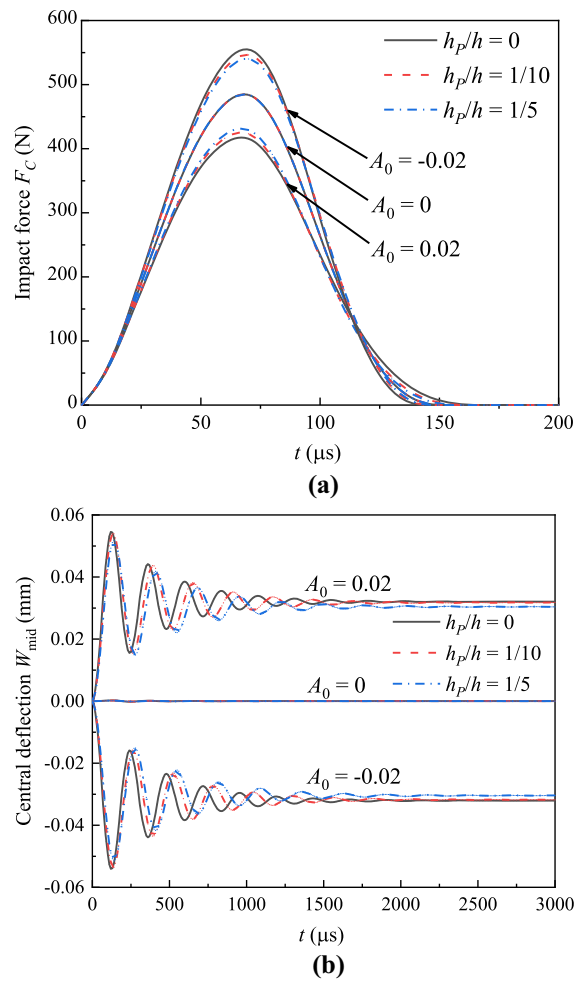


Fig. 11 Effect of thickness ratio on the **a** impact force and **b** impact response of geometrically imperfect X-GRC piezoelectric beam

the impact force F_C increases, and the absolute value of the central deflection W_{mid} decreases.

6 Conclusions

The nonlinear low-velocity impact responses of GRC beam with geometric imperfection under thermo-electro-mechanical loads are investigated. The impact force is calculated by the modified nonlinear Hertz contact law. Based on the first-order shear deformation beam theory, von Kármán nonlinear displacement-strain relationship and Hamilton principle, the nonlinear dynamic equations are deduced, and solved by the DQ method and Newmark- β method combined

with Newton–Raphson iterative method. Comprehensive numerical results are presented to investigate the effects of the distribution pattern and weight fraction of GPLs, the mode and amplitude of imperfection, initial velocity of the spherical impactor, temperature variation, thickness of piezoelectric layer, as well as the coupled effect of geometric imperfection and thermo-electro-mechanical load on the low-velocity impact characteristics of the geometrically imperfect GRC piezoelectric beam. The major conclusions are given as follows.

- (1) When calculating the impact behaviors of geometrically imperfect GRC piezoelectric beam via DQ method, the geometric imperfection with sudden changes require more nodes number. G_1 -mode is the most harmful imperfection for the stability of the GRC piezoelectric beam under impact.
- (2) When GPL reinforcements are distributed into GRC core beam, only FG-X pattern reduces the low-velocity impact response of geometrically imperfect GRC piezoelectric beam. For GPL reinforcements distributing into the piezoelectric layers, all the patterns are effective for reducing the central deflection of the geometrically imperfect GRC piezoelectric beam under impact.
- (3) The thermal load has barely effect on the impact behaviors of intact GRC piezoelectric beam. Once the geometric imperfection appearing, the thermal effect is largely amplified.

Acknowledgements The authors gratefully acknowledge the support of National Natural Science Foundation of China (NNSFC) through Grant Nos. 12172012, 11802005, 11832002 and 11427801, the Funding Project for Academic Human Resources Development in Institutions of Higher Learning under the Jurisdiction of Beijing Municipality (PHRIHLB), the General Program of Science and Technology Development Project of Beijing Municipal Education Commission (KM201910005035), and the Beijing Natural Science Foundation (No.3222006).

Data availability The datasets generated during and analyzed during the current study are available from the corresponding author on reasonable request.

Declarations

Conflict of interest The authors declare that there is no conflict of interests regarding the publication of this paper.

References

1. Farokhi, H., Ghayesh, M.H.: Thermo-mechanical dynamics of perfect and imperfect Timoshenko microbeams. *Int. J. Eng. Sci.* **91**, 12–33 (2015)
2. Mirjavadi, S.S., Afshari, B.M., Barati, M.R., Hamouda, A.M.S.: Nonlinear free and forced vibrations of graphene nanoplatelet reinforced microbeams with geometrical imperfection. *Microsyst. Technol.* **25**(8), 3137–3150 (2019)
3. Farajpour, A., Ghayesh, M.H., Farokhi, H.: Nonlocal nonlinear mechanics of imperfect carbon nanotubes. *Int. J. Eng. Sci.* **142**, 201–215 (2019)
4. Rafiee, M., He, X.Q., Liew, K.M.: Non-linear dynamic stability of piezoelectric functionally graded carbon nanotube-reinforced composite plates with initial geometric imperfection. *Int. J. Non-Linear Mech.* **59**, 37–51 (2014)
5. Jansen, E.L.: The effect of geometric imperfections on the vibrations of anisotropic cylindrical shells. *Thin Walled Struct.* **45**(3), 274–282 (2007)
6. Sheinman, I., Adan, M.: Imperfection sensitivity of a beam on a nonlinear elastic foundation. *Int. J. Mech. Sci.* **33**(9), 753–760 (1991)
7. Farokhi, H., Ghayesh, M.H., Kosasih, B., Akaber, P.: On the nonlinear resonant dynamics of Timoshenko microbeams: effects of axial load and geometric imperfection. *Meccanica* **51**(1), 155–169 (2015)
8. Wadee, M.A.: Effects of periodic and localized imperfections on struts on nonlinear foundations and compression sandwich panels. *Int. J. Solids Struct.* **37**, 1191–1209 (2000)
9. Naebe, M., Shirvanimoghaddam, K.: Functionally graded materials: A review of fabrication and properties. *Appl. Mater. Today* **5**, 223–245 (2016)
10. Zhang, L.W., Selim, B.A.: Vibration analysis of CNT-reinforced thick laminated composite plates based on Reddy's higher-order shear deformation theory. *Compos. Struct.* **160**, 689–705 (2017)
11. Boussoula, A., Boucham, B., Bourada, M., Bourada, F., Tounsi, A., Bousahla, A.A., Tounsi, A.: A simple nth-order shear deformation theory for thermomechanical bending analysis of different configurations of FG sandwich plates. *Smart Struct. Syst.* **25**(2), 197–218 (2020)
12. Jafari, P., Kiani, Y.: Free vibration of functionally graded graphene platelet reinforced plates: a quasi 3D shear and normal deformable plate model. *Compos. Struct.* **275**, 114409 (2021)
13. Nguyen, T.N., Ngo, T.D., Nguyen-Xuan, H.: A novel three-variable shear deformation plate formulation: theory and isogeometric implementation. *Comput. Methods Appl. Mech. Eng.* **326**, 376–401 (2017)
14. Nguyen, L.B., Thai, C.H., Duong-Nguyen, N., Nguyen-Xuan, H.: A size-dependent isogeometric approach for vibration analysis of FG piezoelectric porous microplates using modified strain gradient theory. *Eng. Comput.* (2021). <https://doi.org/10.1007/s00366-021-01468-7>
15. Nguyen, T.N., Thai, C.H., Luu, A.T., Nguyen-Xuan, H., Lee, J.: NURBS-based postbuckling analysis of functionally graded carbon nanotube-reinforced composite shells. *Comput. Methods Appl. Mech. Eng.* **347**, 983–1003 (2019)
16. Rafiee, M., Yang, J., Kitipornchai, S.: Large amplitude vibration of carbon nanotube reinforced functionally graded

- composite beams with piezoelectric layers. *Compos. Struct.* **96**, 716–725 (2013)
17. Rafiee, M., Yang, J., Kitipornchai, S.: Thermal bifurcation buckling of piezoelectric carbon nanotube reinforced composite beams. *Comput. Math. Appl.* **66**(7), 1147–1160 (2013)
 18. Selim, B.A., Liu, Z.S., Liew, K.M.: Active vibration control of functionally graded graphene nanoplatelets reinforced composite plates integrated with piezoelectric layers. *Thin-Walled Structures.* **145**, 106372 (2019)
 19. Selim, B.A., Liu, Z., Liew, K.M.: Active control of functionally graded carbon nanotube–reinforced composite plates with piezoelectric layers subjected to impact loading. *J. Vib. Control* **26**(7–8), 581–598 (2019)
 20. Wu, H.L., Kitipornchai, S., Yang, J.: Thermo-electro-mechanical postbuckling of piezoelectric FG-CNTRC beams with geometric imperfections. *Smart Mater. Struct.* **25**(9), 095022 (2016)
 21. Sritawat, K., Wu, H.L., Yang, J.: Free vibration of thermo-electro-mechanically postbuckled FG-CNTRC beams with geometric imperfections. *Steel Compos. Struct.* (2019).
 22. Novoselov, K.S., Geim, A.K., Morozov, S.V., Jiang, D., Zhang, Y., Dubonos, S.V., Firsov, A.A.: Electric field effect in atomically thin carbon films. *Science* **22**, 666 (2004)
 23. Govorov, A., Wentzel, D., Miller, S., Kanaan, A., Sevostianov, I.: Electrical conductivity of epoxy-graphene and epoxy-carbon nanofibers composites subjected to compressive loading. *Int. J. Eng. Sci.* **123**, 174–180 (2018)
 24. Rafiee, M.A., Rafiee, J., Wang, Z., Song, H., Yu, Z.Z., Koratkar, N.: Enhanced mechanical properties of nanocomposites at low graphene content. *ACS Nano* **3**, 3884–3890 (2009)
 25. Zhao, S.Y., Zhao, Z., Yang, Z.C., Ke, L.L., Kitipornchai, S., Yang, J.: Functionally graded graphene reinforced composite structures: a review. *Eng. Struct.* **210**, 110339 (2020)
 26. Feng, C., Kitipornchai, S., Yang, J.: Nonlinear bending of polymer nanocomposite beams reinforced with non-uniformly distributed graphene platelets (GPLs). *Compos. B Eng.* **110**, 132–140 (2017)
 27. Feng, C., Kitipornchai, S., Yang, J.: Nonlinear free vibration of functionally graded polymer composite beams reinforced with graphene nanoplatelets (GPLs). *Eng. Struct.* **140**, 110–119 (2017)
 28. Wang, Y., Zhou, Y., Feng, C., Yang, J., Zhou, D., Wang, S.: Numerical analysis on stability of functionally graded graphene platelets (GPLs) reinforced dielectric composite plate. *Appl. Math. Model.* **101**, 239–258 (2022)
 29. Wang, Y., Feng, C., Yang, J., Zhou, D., Wang, S.: Nonlinear vibration of FG-GPLRC dielectric plate with active tuning using differential quadrature method. *Comput. Methods Appl. Mech. Eng.* **379**, 113767 (2021)
 30. Mao, J.J., Zhang, W., Lu, H.M.: Static and dynamic analyses of graphene-reinforced aluminium-based composite plate in thermal environment. *Aerosp. Sci. Technol.* **107**, 106354 (2020)
 31. Mao, J.J., Lai, S.K., Zhang, W., Liu, Y.Z.: Comparisons of nonlinear vibrations among pure polymer plate and graphene platelet reinforced composite plates under combined transverse and parametric excitations. *Compos. Struct.* **265**, 113767 (2021)
 32. Mao, J.J., Lu, H.M., Zhang, W., Lai, S.K.: Vibrations of graphene nanoplatelet reinforced functionally gradient piezoelectric composite microplate based on nonlocal theory. *Compos. Struct.* **236**, 111813 (2020)
 33. Mao, J.J., Guo, L.J., Zhang, W.: Vibration and frequency analysis of edge-cracked functionally graded graphene reinforced composite beam with piezoelectric actuators. *Eng. Comput.* (2021). <https://doi.org/10.1007/s00366-021-01546-w>
 34. Safarpour, M., Rahimi, A.R., Alibeigloo, A.: Static and free vibration analysis of graphene platelets reinforced composite truncated conical shell, cylindrical shell, and annular plate using theory of elasticity and DQM. *Mech. Based Des. Struct. Mach.* **48**, 496–524 (2019)
 35. Rahimi, A., Alibeigloo, A., Safarpour, M.: Three-dimensional static and free vibration analysis of graphene platelet–reinforced porous composite cylindrical shell. *J. Vib. Control* **26**, 1627–1645 (2020)
 36. Niu, Y., Yao, M.H.: Linear and nonlinear vibrations of graphene platelet reinforced composite tapered plates and cylindrical panels. *Aerosp. Sci. Technol.* **115**, 106798 (2021)
 37. Niu, Y., Yao, M.H., Wu, Q.L.: Nonlinear vibrations of functionally graded graphene reinforced composite cylindrical panels. *Appl. Math. Model.* **101**, 1–18 (2022)
 38. Wang, Y.W., Fu, T.R., Zhang, W.: An accurate size-dependent sinusoidal shear deformable framework for GNP-reinforced cylindrical panels: applications to dynamic stability analysis. *Thin-Walled Struct.* **160**, 107400 (2021)
 39. Wang, Y.W., Zhang, W.: On the thermal buckling and postbuckling responses of temperature-dependent graphene platelets reinforced porous nanocomposite beams. *Compos. Struct.* **296**, 115880 (2022)
 40. Song, M.T., Li, X.Q., Kitipornchai, S., Bi, Q.S., Yang, J.: Low-velocity impact response of geometrically nonlinear functionally graded graphene platelet-reinforced nanocomposite plates. *Nonlinear Dyn.* **95**(3), 2333–2352 (2018)
 41. Song, M.T., Yang, J., Kitipornchai, S., Zhu, W.D.: Buckling and postbuckling of biaxially compressed functionally graded multilayer graphene nanoplatelet-reinforced polymer composite plates. *Int. J. Mech. Sci.* **131–132**, 345–355 (2017)
 42. Barati, M.R., Zenkour, A.M.: Analysis of postbuckling of graded porous GPL-reinforced beams with geometrical imperfection. *Mech. Adv. Mater. Struct.* **26**(6), 503–511 (2018)
 43. Salehi, M., Gholami, R., Ansari, R.: Analytical solution approach for nonlinear vibration of shear deformable imperfect FG-GPLR porous nanocomposite cylindrical shells. *Mech. Based Des. Struct. Mach.* (2021). <https://doi.org/10.1080/15397734.2021.1891096>
 44. Liu, H., Wu, H., Lyu, Z.: Nonlinear resonance of FG multilayer beam-type nanocomposites: Effects of graphene nanoplatelet-reinforcement and geometric imperfection. *Aerosp. Sci. Technol.* **98**, 105702 (2020)
 45. Fan, Y., Xiang, Y., Shen, H.S., Wang, H.: Low-velocity impact response of FG-GRC laminated beams resting on visco-elastic foundations. *Int. J. Mech. Sci.* **141**, 117–126 (2018)

46. Fan, Y., Xiang, Y., Shen, H.S., Hui, D.: Nonlinear low-velocity impact response of FG-GRC laminated plates resting on visco-elastic foundations. *Compos. B Eng.* **144**, 184–194 (2018)
47. Dong, Y.H., Zhu, B., Wang, Y., He, L.W., Li, Y.H., Yang, J.: Analytical prediction of the impact response of graphene reinforced spinning cylindrical shells under axial and thermal loads. *Appl. Math. Model.* **71**, 331–348 (2019)
48. Selim, B.A., Liu, Z.: Impact analysis of functionally-graded graphene nanoplatelets-reinforced composite plates laying on Winkler-Pasternak elastic foundations applying a meshless approach. *Eng. Struct.* **241**, 112453 (2021)
49. Zhang, L., Chen, Z., Habibi, M., Ghabussi, A., Alyousef, R.: Low-velocity impact, resonance, and frequency responses of FG-GPLRC viscoelastic doubly curved panel. *Compos. Struct.* **269**, 114000 (2021)
50. Yang, S.H., Sun, C.T.: Indentation law for composite laminates. NASA CR-165460. (1981).
51. Wang, S.Y., Quek, S.T., Ang, K.K.: Vibration control of smart piezoelectric composite plates. *Smart Mater. Struct.* **10**, 637–644 (2001)
52. Shu, C.: *Differential quadrature and its application in engineering.* (2000).
53. Wang, Y.W., Xie, K., Fu, T.R., Shi, C.L.: Vibration response of a functionally graded graphene nanoplatelet reinforced composite beam under two successive moving masses. *Compos. Struct.* **209**, 928–939 (2019)
54. Kazemi, M., Rad, M.H.G., Hosseini, S.M.: Nonlinear dynamic analysis of FG carbon nanotube/epoxy nanocomposite cylinder with large strains assuming particle/matrix interphase using MLPG method. *Eng. Anal. Boundary Elem.* **132**, 126–145 (2021)
55. Wang, Y., Feng, C., Wang, X.W., Zhao, Z., Romero, C.S., Dong, Y.H., Yang, J.: Nonlinear static and dynamic responses of graphene platelets reinforced composite beam with dielectric permittivity. *Appl. Math. Model.* **71**, 298–315 (2019)
56. Ibrahim, S.M., Patel, B.P., Nath, Y.: Modified shooting approach to the non-linear periodic forced response of isotropic/composite curved beams. *Int. J. Non-Linear Mech.* **44**(10), 1073–1084 (2009)
57. Ibrahim, S.M., Patel, B.P., Nath, Y.: Nonlinear periodic response of composite curved beam subjected to symmetric and antisymmetric mode excitation. *J. Comput. Nonlinear Dyn.* (2010). <https://doi.org/10.1115/1.4000825>
58. Mahmoodi, M.J., Rajabi, Y., Khodaiepour, B.: Electro-thermo-mechanical responses of laminated smart nanocomposite moderately thick plates containing carbon nanotube-A multi-scale modeling. *Mech. Mater.* **141**, 103247 (2020)
59. Wu, H.L., Yang, J., Kitipornchai, S.: Nonlinear vibration of functionally graded carbon nanotube-reinforced composite beams with geometric imperfections. *Compos. B Eng.* **90**, 86–96 (2016)
60. Jam, J.E., Kiani, Y.: Low velocity impact response of functionally graded carbon nanotube reinforced composite beams in thermal environment. *Compos. Struct.* **132**, 35–43 (2015)

Springer Nature or its licensor holds exclusive rights to this article under a publishing agreement with the author(s) or other rightsholder(s); author self-archiving of the accepted manuscript version of this article is solely governed by the terms of such publishing agreement and applicable law.

Publisher's Note Springer Nature remains neutral with regard to jurisdictional claims in published maps and institutional affiliations.